Article

Coral-like Ti₃C₂Tₓ/PANI Binary Nanocomposite Wearable Enzyme Electrochemical Biosensor for Continuous Monitoring of Human Sweat Glucose

Jinhao Wang [1], **Lijuan Chen** [1,*] , **Fan Chen** [1], **Xinyang Lu** [1], **Xuanye Li** [1], **Yu Bao** [1] , **Wei Wang** [1], **Dongxue Han** [1] and **Li Niu** [1,2,*]

[1] Guangdong Engineering Technology Research Center for Photoelectric Sensing Materials & Devices, Guangzhou Key Laboratory of Sensing Materials & Devices, Center for Advanced Analytical Science, School of Chemistry and Chemical Engineering, Guangzhou University, Guangzhou 510006, China; 2112205024@e.gzhu.edu.cn (J.W.); 1112316013@e.gzhu.edu.cn (F.C.); 32105100044@e.gzhu.edu.cn (X.L.); 32105100080@e.gzhu.edu.cn (X.L.); baoyu@gzhu.edu.cn (Y.B.); wangw@gzhu.edu.cn (W.W.); dxhan@gzhu.edu.cn (D.H.)

[2] School of Chemical Engineering and Technology, Sun Yat-Sen University, Zhuhai 519082, China

* Correspondence: gdchenlj@gzhu.edu.cn (L.C.); lniu@gzhu.edu.cn (L.N.); Tel.: +86-020-39366902 (L.C. & L.N.)

Abstract: With the continuous advancement of contemporary medical technology, an increasing number of individuals are inclined towards self-monitoring their physiological health information, specifically focusing on monitoring blood glucose levels. However, as an emerging flexible sensing technique, continuous and non-invasive monitoring of glucose in sweat offers a promising alternative to conventional invasive blood tests for measuring blood glucose levels, reducing the risk of infection associated with blood testing. In this study, we fabricated a flexible and wearable electrochemical enzyme sensor based on a two-dimensional Ti₃C₂Tₓ MXene nanosheets and coral-like polyaniline (PANI) binary nanocomposite (denoted as Ti₃C₂Tₓ/PANI) for continuous, non-invasive, real-time monitoring of sweat glucose. The exceptional conductivity of Ti₃C₂Tₓ MXene nanosheets, in conjunction with the mutual doping effect facilitated by coral-like PANI, significantly enhances electrical conductivity and specific surface areas of Ti₃C₂Tₓ/PANI. Consequently, the fabricated sensor exhibits remarkable sensitivity ($25.16 \ \mu A \cdot mM^{-1} \cdot cm^{-2}$), a low detection limit of glucose (26 μM), and an extensive detection range (0.05 mM~1.0 mM) in sweat. Due to the dense coral-like structure of Ti₃C₂Tₓ/PANI binary nanocomposite, a larger effective area is obtained to offer more active sites for enzyme immobilization and enhancing enzymatic catalytic activity. Moreover, the sensor demonstrates exceptional mechanical performance, enabling a 60° bend in practical applications, thus satisfying the rigorous demands of human sweat detection applications. The results obtained from continuous 60 min in vitro monitoring of sweat glucose levels demonstrate a robust correlation with the data of blood glucose levels collected by a commercial glucose meter. Furthermore, the fabricated Ti₃C₂Tₓ/PANI/GOx sensor demonstrated agreement with HPLC findings regarding the actual concentration of added glucose. This study presents an efficient and practical approach for the development of a highly reliable MXene glucose biosensor, enabling stable and long-term monitoring of glucose levels in human sweat.

Keywords: sweat; Ti₃C₂Tₓ MXene; glucose detection; wearable biosensor; enzyme

1. Introduction

The chronic nature of diabetes is characterized by inadequate insulin production, resulting in elevated blood glucose levels, which can give rise to a multitude of severe complications including stroke, myocardial infarction, and renal failure [1]. The projected prevalence of diabetes is anticipated to reach 578 million individuals by 2030 [2]. Diabetes remains an incurable condition, emphasizing the criticality of maintaining a stable blood

glucose level for its management [3,4]. However, current conventional methods of blood glucose monitoring rely on commercially portable enzyme glucose meters that necessitate the invasive collection of blood from the fingertips. The discomfort associated with repeated needling elicits anxiety in patients, heightens the risk of wound infection, and engenders resistance towards regular blood glucose monitoring among individuals in their daily lives [5,6]. Consequently, it is an urgent need to develop a blood glucose monitoring device that meets the needs of patients, providing convenience, non-invasiveness, and continuous monitoring of glucose levels. It is well-known that glucose is present in various biological fluids apart from serum, including urine, tears, saliva, and sweat. With the progress of medical care, various wearable non-invasive glucose sensors have been developed and utilized for continuous monitoring of glucose levels [7–10].

Sweat, a metabolite secreted by sweat glands, contains abundant metabolic information such as ions, lactic acid, urea, and glucose. Based on the established correlation between blood and sweat glucose concentrations demonstrated in the previous studies, wearable glucose sensors with unique selectivity, rapid response, and facile miniaturization gained extensive application for sustainable and non-invasive monitoring of sweat glucose concentration [11–13]. Both enzyme sensors and non-enzymatic sensors are employed for the detection of glucose concentration in sweat. Glucose oxidase (GOx) is commonly utilized for the oxidation of glucose, facilitating in direct electron transfer from the enzyme to the electrode. However, due to the inherent instability and low activity of glucose oxidase, enzyme immobilization poses a critical challenge in achieving glucose sensors with superior stability, selectivity, and reproducibility. Therefore, it is imperative to prioritize conductive composite materials that exhibit enhanced catalytic activity and stability for glucose oxidation during the process of glucose oxidase immobilization. Recently, novel nanocomposites were developed for the immobilization of glucose oxidase such as metal–organic framework materials (MOFs), porous nanocomposites, hydrogels, magnetic nanoparticles, carbon nanomaterials, metal, and metal oxide nanoparticles. Song et al. designed a Cu 2D MOFs for the co-immobilization of glucose oxidase (GOx) and horseradish peroxidase (HRP) [14] through adsorption and covalent immobilization strategies with superior enzymatic activity for glucose detection in harsh environments. Guldin et al. constructed the ordered porous aluminosilicate-coated electrodes with different modification protocols for the immobilization of GOx in electrochemical glucose sensing [15]. Among them, amino-modified porous aluminosilicates displayed better sensitivity and wider linear range for electrochemical detection of glucose. Kim et al. prepared poly (vinyl alcohol)/β-cyclodextrin (PVA/β-CD) hydrogels physically immobilized GOx for accurate detection of interstitial fluid glucose levels with high sensitivity and low detection limit at low applied potential [16]. Lin et al. designed a flexible glucose biosensor in human sweat composed of a GOx/N-GQDs/PANI nanocomposite layer for non-invasive human sweat glucose monitoring on a wearable biosensor [17]. Hao et al. prepared a MnO_2/multi-walled carbon nanotubes (MWCNTs) nanocomposite with a simple hydrothermal method and a glucose biosensor was developed by incorporation of GOx [18]. However, the continuous advancement in nanomaterials for efficient immobilization of GOx and rapid glucose detection remains a prominent area of research focus and still presents a significant research challenge.

As a novel two-dimensional (2D) nanomaterial, MXene exhibits exceptional physical and chemical properties, making it as an excellent conductive material suitable for the monitoring of various key biomolecules in sweat, such as glucose, dopamine, and ascorbic acid. MXene nanosheets consisting of Ti_3C_2 layers are exfoliated from the intermediate "A" layers of the MAX phase in hydrofluoric acid. Moreover, the general formula of MXene can be expressed as $M_{n+1}X_nT_x$, where n can take on values of 1, 2, or 3; M represents early transition metals such as Ti, Ta, V, and Nb; T_x indicates surface functional groups carried by etching processes, such as hydroxyl (−OH), chlorine (−Cl), oxide (−O), and fluoride (−F) groups [19,20]. Due to the unique structure and controllable surface chemical composition, excellent conductivity, adjustable hydrophilicity, superior catalytic charac-

teristics, high volumetric capacitance, and specific surface area, $Ti_3C_2T_x$ MXene exhibits promising application prospects in various fields, including electromagnetic shielding, photocatalysis, and biomedical applications and sensors. The applications of MXenes as a tunable sensitive material in sweat sensors are primarily focused on the detection of physiological and biochemical signals such as lactate acid, glucose, uric acid, and protein [21]. However, the interaction between van der Waals forces and hydrogen bonds in the $Ti_3C_2T_x$ MXene monolayer leads to a reduction in surface area and constraining the electrochemical sensor performance of $Ti_3C_2T_x$ [22,23]. Therefore, the introduction of specific components to generate the intercalation and bridging effects is essential to improve the conductivity and avoid the issue of layer stacking of $Ti_3C_2T_x$ MXene [24,25]. In addition, the newly incorporated components must possess enhanced electrochemical characteristics and intrinsic conductivity and be able to synergize with MXene to enhance the detection of biological analytes.

Herein, this study presents a long-term stable, flexible sensing platform based on an active catalytic binary composite by incorporating coral-like polyaniline on the $Ti_3C_2T_x$ nanoflake surface to improve the stability, specific surface area, and conductivity of $Ti_3C_2T_x$, thereby amplifying the immobilization impact of the enzyme by increasing active sites for highly sensitive, selective, and accurate glucose monitoring in sweat. The working electrode of the glucose biosensor was constructed with the $Ti_3C_2T_x$/PANI electrocatalytic transduction layer through aniline electropolymerized on the $Ti_3C_2T_x$ surface, and finally functionalized with glucose oxidase. Compared to neat $Ti_3C_2T_x$ and PANI, the $Ti_3C_2T_x$/PANI binary nanocomposite-modified electrode demonstrated superior catalytic activity, lower detection limit, and higher sensitivity in glucose detection of PBS, artificial sweat, and human sweat. The bending test showed that the $Ti_3C_2T_x$/PANI/GOx electrode possessed high mechanical and current response stability. Indeed, we constructed a portable sensor for glucose monitoring in sweat and employed it during exercise. The developed glucose biosensor was utilized for real-time monitoring of sweat glucose in vitro, successfully establishing a robust correlation between blood glucose levels and sweat glucose levels.

2. Material and Methods

2.1. Material and Reagents

Glucose oxidase, potassium chloride (KCl), and sodium chloride (NaCl, purity >99%) were obtained from Sigma Aldrich Trading Co., Ltd., (Shanghai, China). Titanium aluminum carbide (Ti_3AlC_2) MXene powder (98%, 400 mesh) was purchased from 11 Technology Co., Ltd. (Jilin, China). Dopamine (DA, purity 99%), DL-lactic acid, glutaraldehyde (50 wt % aqueous solution), hydrofluoric acid (HF), uric acid (UA, purity 99%), and ascorbic acid (AA, purity > 99%) were obtained from Shanghai Macklin Biochemical Technology Co., Ltd., (Shanghai China). Chitosan (medium viscosity, 200~400 mPa·s), bovine serum albumin (BSA, purity 98%, derived from bovine serum), polyaniline (PANI), aniline (purity >99.5%), glycine, potassium phosphate dibasic (K_2HPO_4), N-methyl-2-pyrrolidinone (NMP), potassium phosphate monobasic (KH_2PO_4), and urea were purchased from Aladdin Scientific Corp, Shanghai, China. The commercial electrode was obtained from Shenzhen Haoyang Technology Co., Ltd, China. KH_2PO_4, K_2HPO_4, and NaCl were used to prepare PBS buffer (0.1 M, pH = 7.4) as a solvent for glucose oxidase and glucose dissolution. All chemicals do not require further purification and all the aqueous solutions were prepared with ultrapure water.

2.2. Preparation $Ti_3C_2T_x$ MXene

$Ti_3C_2T_x$ MXene was prepared according to the previously reported method [21]. Initially, 15 mL of HF was introduced into a Teflon vessel and stirred at 80 rpm in a 0 °C ice bath. Subsequently, 1.5 g of Ti_3AlC_2 powder was gradually added to the HF solution over a duration of 10 min. Following the powder addition, dry nitrogen was introduced into the Teflon vessel to remove air. The suspension was then stirred at 80 rpm for 48 h at

room temperature to ensure complete removal of the Al layer. The suspension was washed repeatedly with ultrapure water and centrifuged at 5000 rpm for 5 min until the pH value exceeded 6. Ultimately, $Ti_3C_2T_x$ MXene powder was obtained by vacuum freeze-drying for 48 h.

2.3. Preparation of $Ti_3C_2T_x$/PANI/GO_x-Based Electrodes

Coral-like PANI-functionalized $Ti_3C_2T_x$ ($Ti_3C_2T_x$/PANI) was obtained by an electrochemical polymerization method. Initially, 10 mg of the prepared $Ti_3C_2T_x$ powder and 1 mL of Nafion solution were dispersed in 9 mL of NMP solution, followed by sonication for 2 h at 25 °C (sonication power of 120 W and frequency of 40 kHz). Subsequently, 8 μL of the mixed solution was taken and added dropwise to the working electrode (5 mm glassy carbon electrode and flexible electrode) and dried at 60 °C for 6 h. Next, the commercial electrode was immersed in aniline (0.25 M) and sulfuric acid (0.5 M) solution to electropolymerize and facilitate the growth of coral-like PANI on the surface of $Ti_3C_2T_x$ via the cyclic voltammetry method with a voltage range from −0.45 V to −0.9 V and a scan rate of 30 mV/s for a total number of twenty cycles. After electropolymerization, the working electrode was washed with ultrapure water to remove residual sulfuric acid and air-dried for 6 h. Subsequently, a mixture containing 10 mg/mL BSA solution, 25 mg/mL GOx, 2 mg/mL chitosan solution, and a 1.0 wt % glutaraldehyde solution in PBS was prepared in a ratio of 2:4:1:1. The mixed solution (8 μL) was dropwise added onto the surface of the $Ti_3C_2T_x$/PANI electrode and incubated at 4 °C for 12 h for enzyme immobilization. Finally, a droplet of Nafion solution was added onto the flexible sensor to obtain the $Ti_3C_2T_x$/PANI/GOx glucose sensor (the schematic illustration of the preparation of $Ti_3C_2T_x$/PANI/GOx flexible glucose biosensor is demonstrated in Figure 1a). The obtained glucose sensor was stored at 4 °C for one day before use. As control tests, $Ti_3C_2T_x$/GOx biosensors and PANI/GOx biosensors were also prepared and stored at 4 °C before use.

2.4. Materials Characterization

The morphologies and chemical structures of MXene and $Ti_3C_2T_x$/PANI were investigated by scan electron microscopy (SEM, JEOL, and JSM-7001F) and transmission electron microscopy (TEM, JEOL, and JEM-2100) (Tokyo, Japan). The structure of samples is analyzed using X-ray diffraction (XRD) (Bruker D8 ADVANCE, Billerica, MA, USA). X-ray photoelectron spectroscopy (XPS) measurements were performed using the Thermo Scientific K-Alpha system manufactured by Thermo Fisher Scientific in the United States (Waltham, MA, USA). Raman spectra were measured by using a LabRAM HR800 instrument with a laser excitation from the Nd: YAG laser source at 532 nm.

2.5. Electrochemical Characterization

Electrochemical measurement and glucose concentration measurement were performed with Gamry workstation and CHI 760E electrochemical workstation, including cyclic voltammetry (CV), chronoamperometry. The current-time curve was obtained at −0.35 V. Electrochemical impedance (EIS) was measured in the 1 MHz to 1 Hz frequency range.

2.6. Electrochemical Characterization in PBS and Artificial Sweat

The electrochemical performance of $Ti_3C_2T_x$/GOx, PANI/GOx, and $Ti_3C_2T_x$/PANI/GOx-modified electrodes was investigated in different glucose concentrations at a scan rate of 50 mV/s, respectively. Glucose in PBS and artificial sweat (pH = 6.5) was determined by chronoamperometry. Under the addition of 0.1 mM AA, 0.5 mM urea, 50 μM UA, 0.05 mM dopamine, 10 mM NaCl, 10 mM KCl, and 0.1 mM glycine, the selectivity of $Ti_3C_2T_{x/}$PANI/Gox glucose sensor in artificial sweat was measured by chronoamperometry.
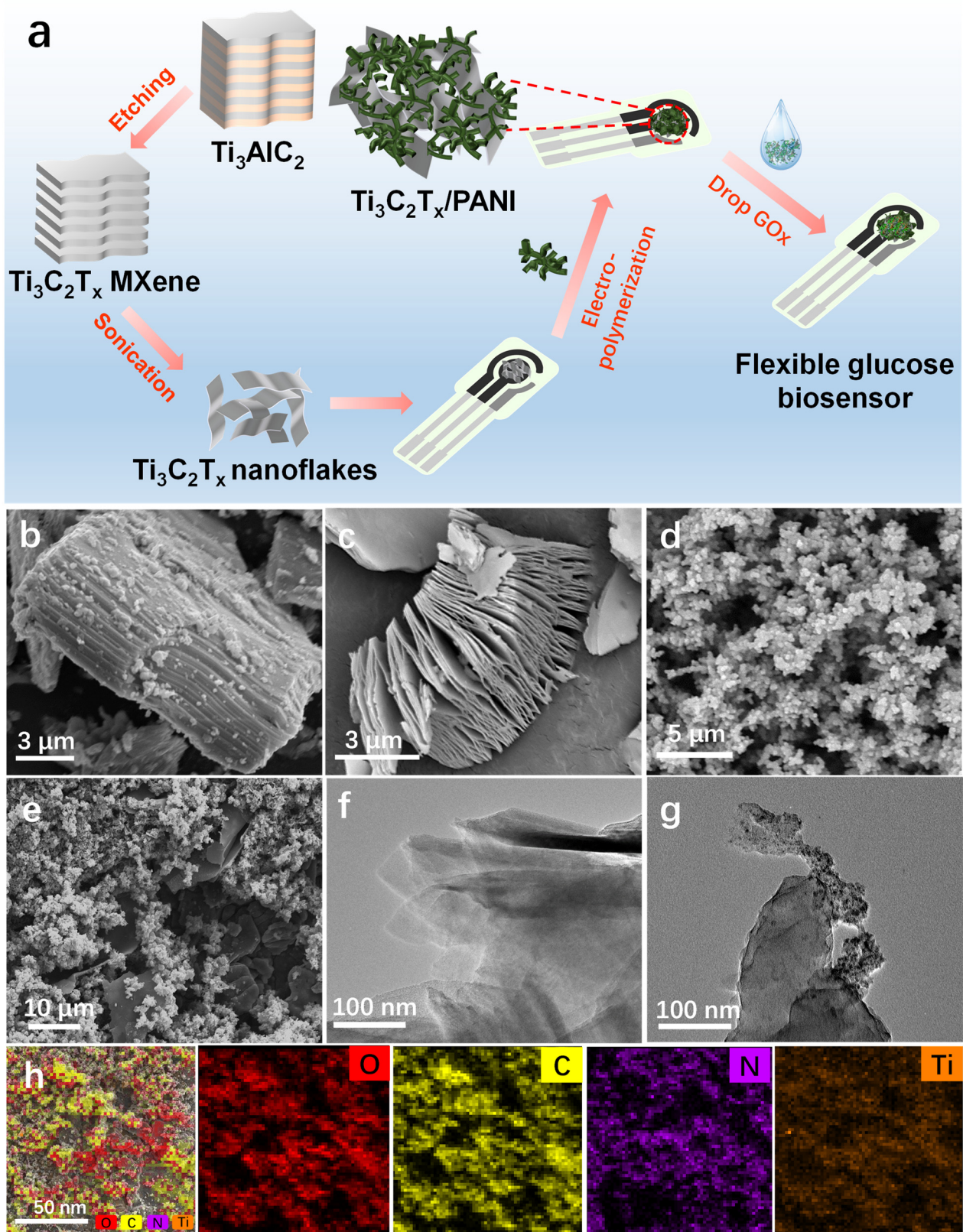
Figure 1. (**a**) Schematic illustration of the preparation of $Ti_3C_2T_x$, $Ti_3C_2T_x$/PANI, and the flexible $Ti_3C_2T_x$/PANI/GOx flexible glucose biosensor; SEM images of (**b**) Ti_3AlC_2 powder; (**c**) $Ti_3C_2T_x$, (**d**) electropolymerized coral-like PANI; and (**e**) $Ti_3C_2T_x$/PANI binary nanocomposite; TEM images of (**f**) $Ti_3C_2T_x$ and (**g**) $Ti_3C_2T_x$/PANI; and (**h**) EDS mapping of $Ti_3C_2T_x$/PANI.

2.7. Electrode Bending Tests

The prepared $Ti_3C_2T_x$/PANI/GOx flexible electrode was subjected to bend at angles of 0°, 30°, and 60°, respectively, and different concentrations of glucose (0~1.0 mM) were examined at different bending angles to evaluate the electrode current changes before and after bending and the stability of the electrode.

2.8. On-Body Measurements

On-body glucose monitoring in sweat was conducted on two healthy subjects aged 20 to 30 years. The glucose sensor ($Ti_3C_2T_x$/PANI/GOx flexible electrode) was securely affixed on the epidermis of the arm, and the electrode had a fixed contact connection to a mini-type equipment function as an electrochemical workstation for real-time glucose monitoring. During the on-body sweat glucose monitoring, the volunteers followed prescribed exercise and dietary instructions. Meanwhile, the invasive blood glucose measurements were obtained using a commercially available conventional glucose meter for comparison with the sweat glucose levels.

3. Results and Discussions

3.1. Morphology of $Ti_3C_2T_x$/PANI

The morphology and surface structure of coral-like $Ti_3C_2T_x$/PANI were observed by SEM and TEM. The unetched pristine Ti_3AlC_2 powder showed a bulk-shaped MAX phase (Figure 1b); after etching the Al layer from Ti_3AlC_2 powder, a two-dimensional layered accordion-like structure of $Ti_3C_2T_x$ was obtained (Figure 1c). Coral-like PANI was fabricated by the electrochemical polymerization method, as shown in Figure 1d. Through electrochemical polymerization of the aniline monomer on the surface of $Ti_3C_2T_x$ nanoflakes, the $Ti_3C_2T_x$/PANI binary nanocomposite with coral-like shape was obtained, as shown in Figure 1e. TEM images of $Ti_3C_2T_x$ and $Ti_3C_2T_x$/PANI are presented in Figure 1f,g, respectively. Obviously, a lamellar shape could be observed at the edges of the etched $Ti_3C_2T_x$ nanoflakes. After electrochemical polymerization of aniline monomer on the $Ti_3C_2T_x$ surface, the surface roughness of the $Ti_3C_2T_x$ nanoflake was significantly increased and the coral-like shape of PANI was grown on a $Ti_3C_2T_x$ nanoflake surface to form a binary nanocomposite $Ti_3C_2T_x$/PANI. Figure S1 shows the HRTEM image of the $Ti_3C_2T_x$/PANI, and the measured lattice fringes pitch was 10.02 Å corresponding to (002) planes of $Ti_3C_2T_x$, matching with the XRD results well. However, the crystal structure of polyaniline was not presented due to its susceptibility to structural damage when exposed to high-intensity electron beams, resulting in the destruction of the crystal structure. The elements of $Ti_3C_2T_x$/PANI were also determined via EDS analysis (Figure 1h), and a uniform distribution of Ti, C, and N elements was detected, which was consistent with the expected results.

3.2. Characterization of $Ti_3C_2T_x$/PANI

XRD patterns of $Ti_3C_2T_x$, PANI, and $Ti_3C_2T_x$/PANI binary nanocomposites were characterized in Figure 2a. The characteristic peaks at 8.9°, 18.1°, 27.5°, 35.1°, 41.8°, and 60.6° were corresponded to the (002), (004), (006), (008), (010), and (110) planes of $Ti_3C_2T_x$, respectively [26,27]. Due to the Al layer etching, the (104) peak at 38.8° was greatly weakened for $Ti_3C_2T_x$. The peaks at 20.8° and 25.3° were the (020) and (200) crystal planes of the emeraldine salt form of the coralline PANI [28]. The intensity of the characteristic peak of (002) of $Ti_3C_2T_x$/PANI was decreased with the growth of the coral-like PANI, indicating that the PANI successfully inserted into the $Ti_3C_2T_x$ lamellae and affected its crystallinity. Furthermore, other characteristic peaks of (020) and (200) crystal planes of the coralline PANI could be detected in the spectrum of $Ti_3C_2T_x$/PANI, indicating that the $Ti_3C_2T_x$/PANI binary nanocomposite successfully prepared. Figure 2b represented Raman spectra of $Ti_3C_2T_x$, PANI, and the $Ti_3C_2T_x$/PANI binary nanocomposite. In the pure $Ti_3C_2T_x$ spectrum, four primary Raman shifts located at 152, 255, 402, and 601 cm^{-1} were observed, respectively. Among them, the fitting peak located at 255 cm^{-1} corresponded to

the out-of-plane vibration of Ti and C atoms at A_{1g} Raman-active mode, the fitting peaks located at 402 cm^{-1} and 601 cm^{-1} corresponded to the in-plane vibration of Ti and C atoms at E_{1g} and E_{2g} Raman-active modes, respectively [29]. Furthermore, the Raman spectrum of $Ti_3C_2T_x$/PANI exhibited distinct fitting peaks at 1338 cm^{-1} and 1571 cm^{-1} similar with the PANI spectrum, indicating successful integration between PANI and $Ti_3C_2T_x$.
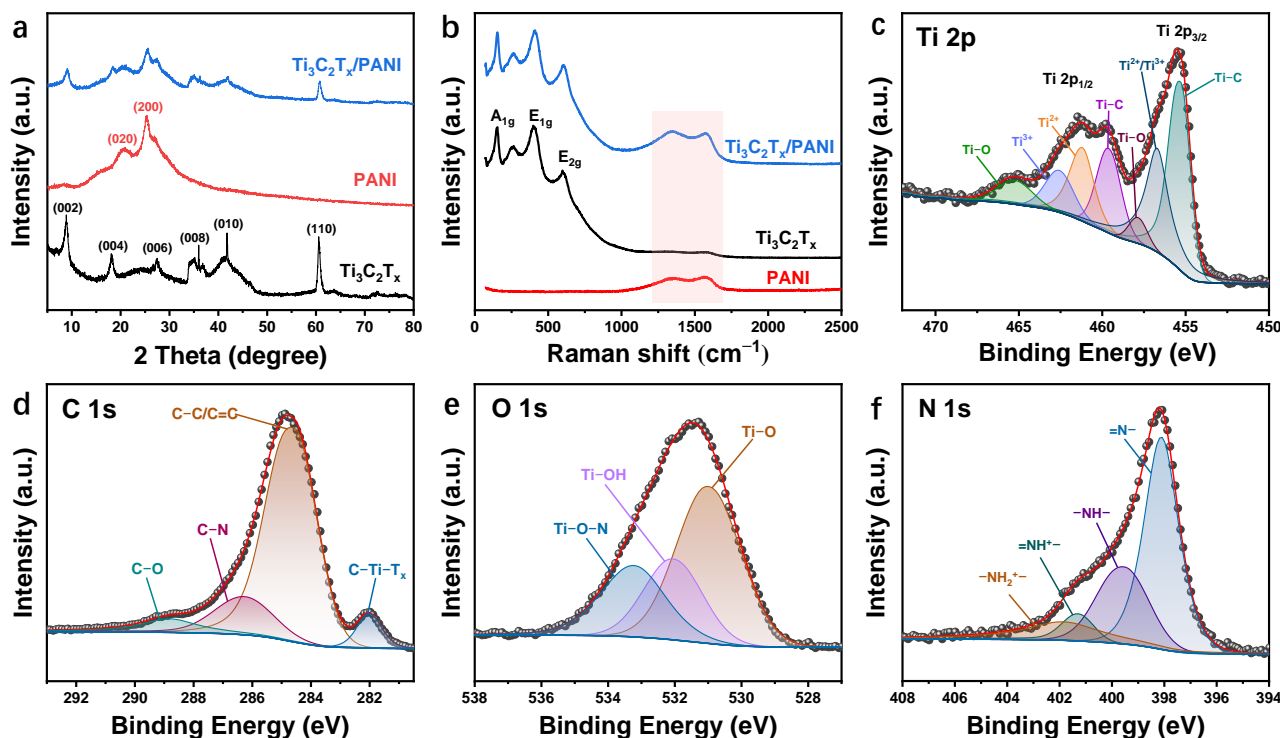

Figure 2. (**a**) XRD patterns and (**b**) Raman spectra of $Ti_3C_2T_x$, PANI and $Ti_3C_2T_x$/PANI powders; XPS spectra of (**c**) Ti 2p; (**d**) C 1s; (**e**) O 1s; and (**f**) N 1s of $Ti_3C_2T_x$/PANI, respectively.

XPS survey spectrum of $Ti_3C_2T_x$/PANI binary nanocomposite was demonstrated in Figure S2, indicating the presence of Ti, C, N, and O elements. The high-resolution spectra of Ti 2p, C 1s, O 1s, and N 1s of $Ti_3C_2T_x$/PANI are fitted in Figure 2c–f, respectively. As shown in Figure 2c, the Ti 2p spectrum demonstrated fitting peaks at 455.4, 456.7, and 457.9 eV of Ti $2p_{3/2}$ were assigned to Ti−C, Ti^{2+}/Ti^{3+}, and Ti−O, respectively, suggesting that the $Ti_3C_2T_x$ was slightly oxidized during the etching process. The fitting peaks detected at 459.7, 461.2, 462.7, and 465.3 eV of the Ti $2p_{1/2}$ spectra were corresponded to Ti−C, Ti^{2+}, Ti^{3+}, and Ti−O, respectively [30,31]. The C 1s spectrum (Figure 2d) of $Ti_3C_2T_x$/PANI was fitted by four peaks located at 282.1, 284.7, 286.3, and 289.0 eV, respectively, and corresponding to C−Ti−T_x, C−C/C=C, C−N, and C−O bond [32,33]. The existence of the C−N bond was attributed to the electro-polymerization of aniline monomers on the $Ti_3C_2T_x$ surface. Furthermore, the fitting peaks at 531.1, 532.1, and 533.3 eV of O1s (Figure 2e) were corresponded to Ti−O, Ti−OH, and Ti−O−N, respectively, indicating a slight oxidation of the $Ti_3C_2T_x$ etching process and the interaction between $Ti_3C_2T_x$ and polyaniline, which further confirmed the successful anchoring of PANI on the $Ti_3C_2T_x$ surface [31–33]. The N 1s spectrum (Figure 2f) of $Ti_3C_2T_x$/PANI could be fitted with four deconvoluted primary peaks at 398.1, 399.6, 401.3, and 402.0 eV, equivalent to =N−, −NH−, =NH$^+$−, and −NH$_2^+$−, respectively [34,35]. These XPS results indicate the successful formation of $Ti_3C_2T_x$/PANI binary nanocomposite.

3.3. Electrochemical Behaviors of the Fabricated Electrodes

The electrochemical behavior of $Ti_3C_2T_x$/GOx, PANI/GOx, and $Ti_3C_2T_x$/PANI/GOx electrodes was investigated by changing the scan rates (10~100 mV/s) and the correspond-

ing CV curves are shown in Figure 3. All the peak currents of $Ti_3C_2T_x$/GOx, PANI/GOx, and $Ti_3C_2T_x$/PANI/GOx electrodes exhibited an increase as the scan rate increased, and the peak potentials of all the modified electrodes indicated the presence of a quasi-reversible redox reaction (Figure 3a–c) [36]. Figure 3d demonstrates a linear relationship between the peak current of all electrodes and the square root of the corresponding scan rate, indicating a typical diffusion-controlled electron transfer process [37]. Furthermore, the electron transfer rates between the immobilized GOx on $Ti_3C_2T_x$, PANI, and $Ti_3C_2T_x$/PANI electrodes during the chemical reaction was calculated according to the Laviron formulation Equations (1) and (2) as follows [38]:

$$E_{p,c} = E^{0\prime} - \frac{2.3RT}{\alpha nF} \log\left[\frac{\alpha nFv}{RTk_s}\right] \tag{1}$$

$$E_{p,a} = E^{0\prime} - \frac{2.3RT}{(1-\alpha)nF} \log\left[\frac{(1-\alpha)nFv}{RTk_s}\right] \tag{2}$$

where T represents temperature in Kelvin, F represents Faraday constant, and R represents the ideal gas constant. Furthermore, n represents the number of transferred electrons, α represents the electron transfer coefficient, and v represents the scan rate, and $E^{0\prime}$ is the formal redox potential. $E_{p,c}$ and $E_{p,a}$ represent the peak potential value at the cathode and anode, respectively. The constant k_s represents the electron exchange rate. The determination of electron transfer parameters (α and k_s) is conducted by constructing Laviron plots, which involved plotting E_p vs. the logarithm of the scan rate. After calculated, the coefficient of electron transfer (α) was 0.58, 0.53, and 0.40 for the $Ti_3C_2T_x$/GOx, PANI/GOx, and $Ti_3C_2T_x$/PANI/GOx electrodes, respectively, while the rate constants for electron exchange (k_s) are determined to be 0.815 s^{-1}, 0.951 s^{-1}, and 1.17 s^{-1}, respectively. The highest k_s value based on the $Ti_3C_2T_x$/PANI/GOx electrode indicated that the coral-like polyaniline decorating on the $Ti_3C_2T_x$ surface enhances the electron transfer between GOx and the electrode. In general, a higher electronic transfer rate of the electrode corresponded to a lower resistance rate of the materials for electrode. The technique of electrochemical impedance spectroscopy (EIS) is highly valuable for monitoring the kinetics and processes occurring at the electrode interface [21]. The Nyquist plots were fitted both before and after the introduction of GOx to the electrodes, accompanied by corresponding equivalent circuit diagrams. As illustrated in Figure S3a,b, the corresponding equivalent circuits consist of electrolyte resistance (Rs) and charge transfer resistance (Rct). Figure S3c demonstrates that both before and after immobilized with GOx, the $Ti_3C_2T_x$/PANI-modified electrodes exhibit the lowest Rct values (13.2 Ω and 71.2 Ω), which are significantly lower than those observed for $Ti_3C_2T_x$-modified electrodes (19.8 Ω and 139.8 Ω) and PANI-modified electrodes (28.3 Ω and 171.2 Ω). The minimal Rct suggests that $Ti_3C_2T_x$/PANI nanocomposites possess enhanced charge conversion efficiency. According to previous reports, the enhancement of the electron transfer rate usually led to an enhancement in the catalytic activity for glucose oxidation [39]. Therefore, the increased electronic exchange rate of the $Ti_3C_2T_x$/PANI electrode might lead to an enhancement in its catalytic activity for glucose.

3.4. The Electrocatalytic Behavior of Glucose on Fabricated Electrodes

The catalytic oxidation of glucose on the fabricated electrodes are observed through CV scans at a scan rate of 50 mV·s^{-1} (Figure S4). In a stirred condition, different concentrations of glucose solutions were added to the PBS solution in sequence to obtain a uniform dispersion of glucose. Due to the different electrode materials, the recorded potentials for the $Ti_3C_2T_x$/GOx electrode (Figure S4a) and $Ti_3C_2T_x$/PANI/GOx electrode (Figure S4c) ranged from −0.6 V to 0.6 V, and −1 V to 1 V for the PANI/GOx electrode (Figure S4b). The calibration curves for anodic and cathodic peak currents versus glucose concentrations of the $Ti_3C_2T_x$/PANI/GOx electrode measured in the CV mode are shown in Figure S4d. The $Ti_3C_2T_x$/PANI/GOx electrode exhibited a more pronounced linearity compared to $Ti_3C_2T_x$/GOx and PANI/GOx electrodes. As the glucose concentration increases, the

current at the anode and cathode gradually increased, indicating the presence of glucose electrocatalytic oxidation behavior on the fabricated electrodes. The electrochemical reaction that is typically occurring at the fabricated electrode could be represented as follows Equation (3) [40]:

$$\text{glucose} + O_2 \overset{GOx}{\rightarrow} \text{gluconic acid} + H_2O_2 \tag{3}$$
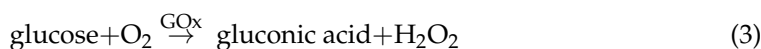
The detection of glucose in the CV mode was accomplished by detecting the signals of hydrogen peroxide oxidation, which were generated due to an enzymatic reaction between glucose oxidase and glucose.
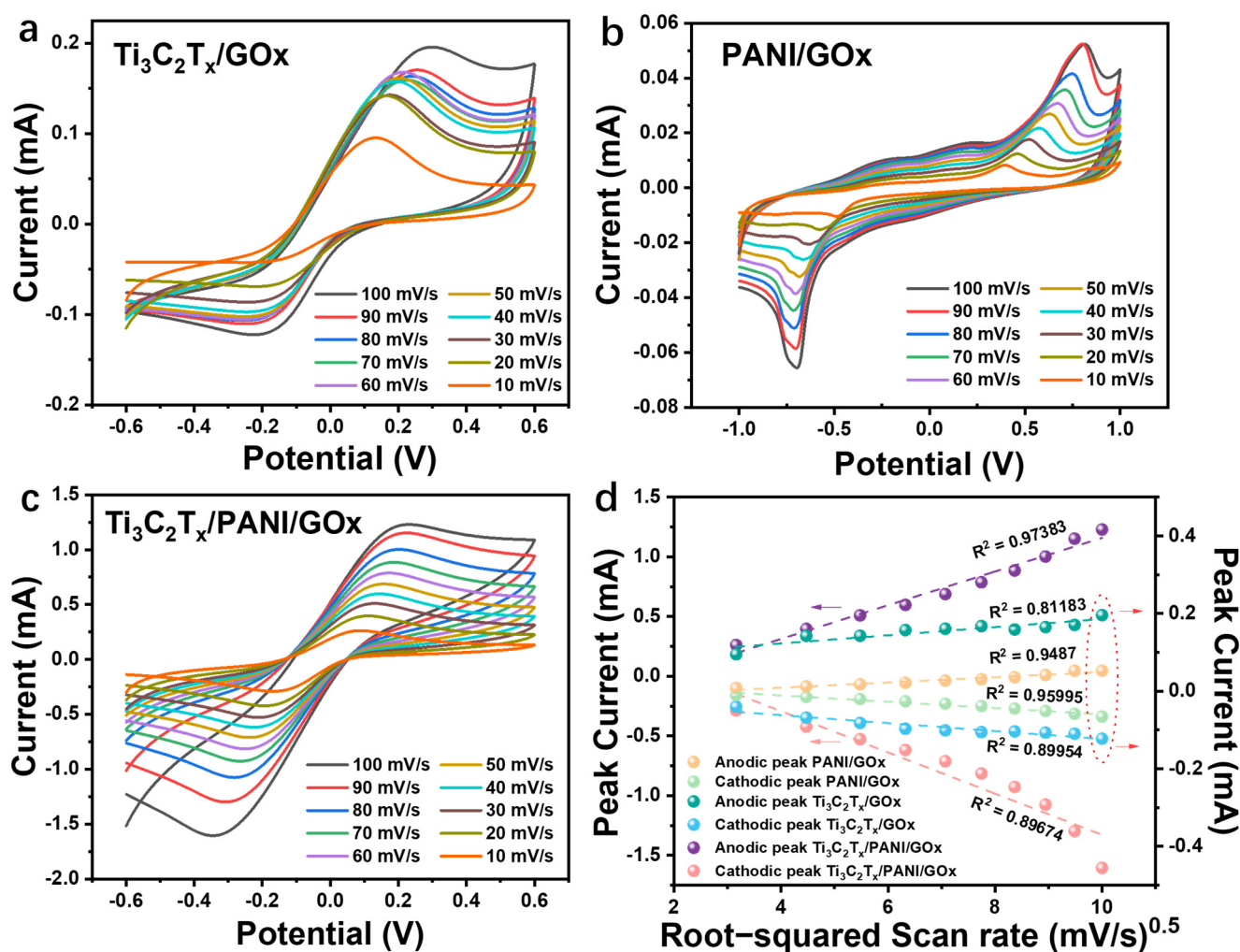
Figure 3. CV curves of (**a**) $Ti_3C_2T_x$/GOx electrode; (**b**) PANI/GOx electrode; (**c**) $Ti_3C_2T_x$/PANI/GOx electrode in PBS containing 0.3 mM glucose at different scan rates from 10 to 100 mV/s, respectively; and (**d**) the calibration plots of the anodic and cathodic peak currents vs. the root-squared scan rate for the different GOx electrode.

To comprehensively compare the electrocatalytic performance of the fabricated electrodes, chronoamperometry measurement was investigated. The chronoamperometry curves of the $Ti_3C_2T_x$/GOx, PANI/Gox, and $Ti_3C_2T_x$/PANI/GOx electrodes in the range of glucose concentration from 0.05 to 2 mM were presented in Figure 4a–c, respectively. All the fabricated electrodes exhibited a stepwise increase in response current for each concentration and indicate rapid diffusion of glucose on the electrode surface. Figure 4d shows the linear calibration curve for the stairs-like chronoamperometry curves, which demonstrates the relationship between glucose concentration and current density. The sensitivities of $Ti_3C_2T_x$/GOx, PANI/GOx and $Ti_3C_2T_x$/PANI/GOx electrodes to glucose

were determined based on the curve slope and calculated to be 8.59 $\mu A \cdot mM^{-1} \cdot cm^{-2}$, 16.52 $\mu A \cdot mM^{-1} \cdot cm^{-2}$, and 26.04 $\mu A \cdot mM^{-1} \cdot cm^{-2}$, respectively. The estimated limits of detection (LOD, S/N = 3) for glucose were as follows [5]: 33 μM for $Ti_3C_2T_x$/GOx, 26 μM for PANI/GOx, and 21 μM for $Ti_3C_2T_x$/PANI/GOx. Compared with $Ti_3C_2T_x$/GOx and PANI/GOx, the $Ti_3C_2T_x$/PANI/GOx exhibited higher sensitivity and lower LOD, which could be attributed to the higher electron conductivity rate and the larger electrode effective area of the coral-like $Ti_3C_2T_x$/PANI binary nanocomposite, which enhanced the enzyme immobilization effect. A comparison of the performance of the $Ti_3C_2T_x$/PANI/GOx glucose sensor with previously reported glucose sensors is presented in Table S1 [41–49]. The sensitivity and LOD of the $Ti_3C_2T_x$/PANI/GOx exhibited competitiveness comparable to that of other reported glucose sensors.

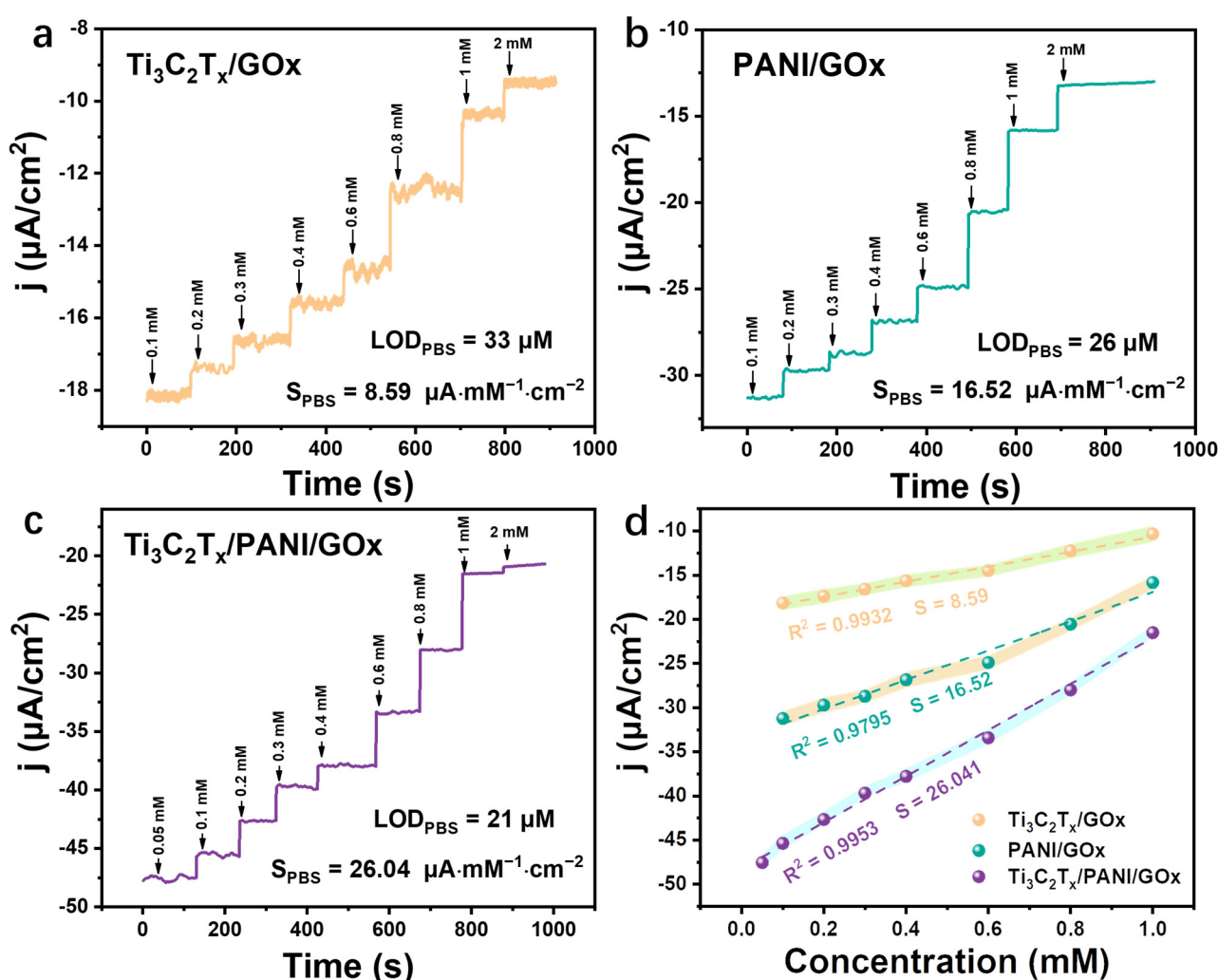**Figure 4.** Chronoamperometry curves of (**a**) $Ti_3C_2T_x$/GOx electrode; (**b**) PANI/GOx electrode; (**c**) $Ti_3C_2T_x$/PANI/GOx electrode; and (**d**) calibration curves of the GOx fabricated electrodes.

3.5. Artificial Sweat Detection

The electrochemical analysis of the $Ti_3C_2T_x$/PANI/GOx sensor in artificial sweat is depicted in Figure 5. Based on the fluctuation range of glucose concentration in human sweat, different concentrations of glucose were successively added to the artificial sweat, and simultaneously amperometric detection was performed. In artificial sweat, the glucose sensor had a detection range from 0.05 to 1.0 mM. As demonstrated in Figure 5a, the current density and glucose concentration show a well-known stair-like behavior. According to the calibration curve of the $Ti_3C_2T_x$/PANI/GOx sensor (Figure 5b), the sen-

sitivity of the sensor to glucose detection was 25.16 $\mu A \cdot mM^{-1} \cdot cm^{-2}$. The selectivity of the $Ti_3C_2T_x$/PANI/GOx sensor was investigated by measuring the current response for 0.3 mM glucose in comparison to other interfering substances commonly found in human sweat. The result demonstrated in Figure 5c verifies that the introduction of interfering substances had a minimal interference with the current response of the sensor, suggesting that the interaction between coral-like PANI and $Ti_3C_2T_x$ promoted the specific recognition of GOx with glucose. Furthermore, the long-term stability of the $Ti_3C_2T_x$/PANI/GOx sensor for glucose detection is represented in Figure 5d,e. Figure 5d shows the continuous amperometric monitoring with $Ti_3C_2T_x$/PANI/GOx glucose sensors to detect 0.6 mM of glucose within 15 h, with insignificant changes in current density (<1.2 $\mu A \cdot mM^{-1} \cdot cm^{-2}$) over the test time. The long-term stability of the $Ti_3C_2T_x$/PANI/GOx sensor was evaluated over a 10-day period, with daily testing conducted (Figure 5e). Subsequently, the electrodes were rinsed in PBS and deionized water before being stored at 4 °C for further testing. The deviation of the current density over a period of 10 days was around 10%, indicating the long-term stability of the $Ti_3C_2T_x$/PANI/GOx sensor. Furthermore, the performance of the enzyme sensor was easily influenced by temperature [50]. Figure 5f shows that the current response of the fabricated glucose sensor increased as the temperature raised from 20 °C to 40 °C, indicating an increase in enzyme activity [51]. The current response of the $Ti_3C_2T_x$/PANI/GOx sensor exhibited a more pronounced change compared to the $Ti_3C_2T_x$/GOx and PANI/GOx sensors. This could be attributed to the dense coral-like structure of $Ti_3C_2T_x$/PANI binary nanocomposite, providing a larger effective area, thereby offering more active sites for enzyme immobilization and enhancing enzymatic catalytic activity. The same preparation method was carried on to fabricate eight $Ti_3C_2T_x$/PANI/GOx glucose sensors for reproducibility in a PBS solution containing 0.3 mM glucose. As depicted in Figure S5, the maximum deviation of current density was approximately 10%, demonstrating the reproducibility of the sensors.
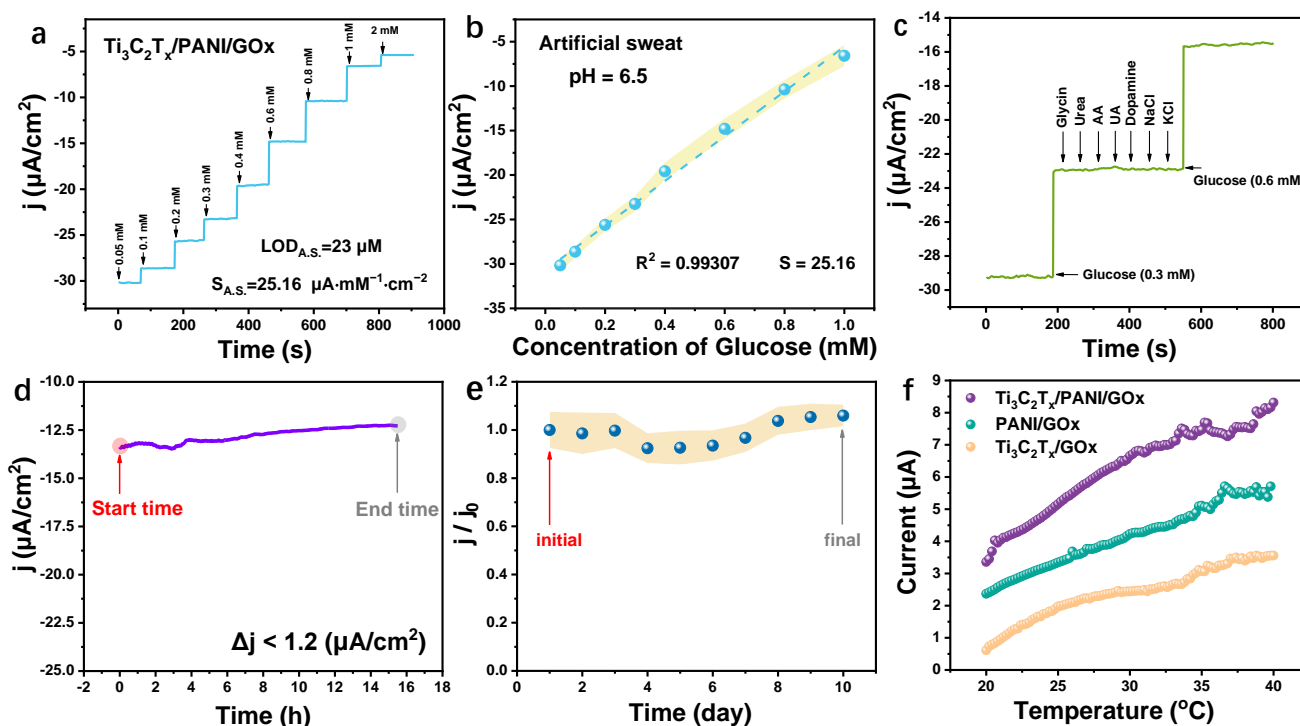

Figure 5. (**a**) Current response of the $Ti_3C_2T_x$/PANI/GOx glucose sensor in different glucose concentrations; (**b**) calibration curve of current density vs. concentration of glucose; (**c**) the anti-interference performance of the $Ti_3C_2T_x$/PANI/GOx sensor; (**d**,**e**) the long-term stability of the $Ti_3C_2T_x$/PANI/GOx sensor; and (**f**) the effect of temperature on glucose sensors.

3.6. On Body Monitoring of Human Sweat Glucose

The wearable $Ti_3C_2T_x$/PANI/GOx sensor contains a lithium-ion battery, a mini-type amperometer, and a $Ti_3C_2T_x$/PANI/GOx flexible chip (Figure 6a). The on-body monitoring of glucose in sweat was demonstrated by directly fixing the integrated sensing platform on the subject's arm during exercise. Due to the unevenness of the upper and lower arm, the flexible chip attached to the skin, bending at a certain angle. The sensing performance of the $Ti_3C_2T_x$/PANI/GOx sensor was explored when bending at $0°$, $30°$, and $60°$, respectively. These bending angles were enough to allow the sensor to be seamlessly attached on body skin. Figure 6b illustrates the relative change in sensor current response, where j and j_0 represent the current densities before and after bending is applied. The maximum relative deviation of the current response for the $Ti_3C_2T_x$/PANI/GOx sensor at a $60°$ angle was approximately 10%, indicating an excellent mechanical property during wearing.
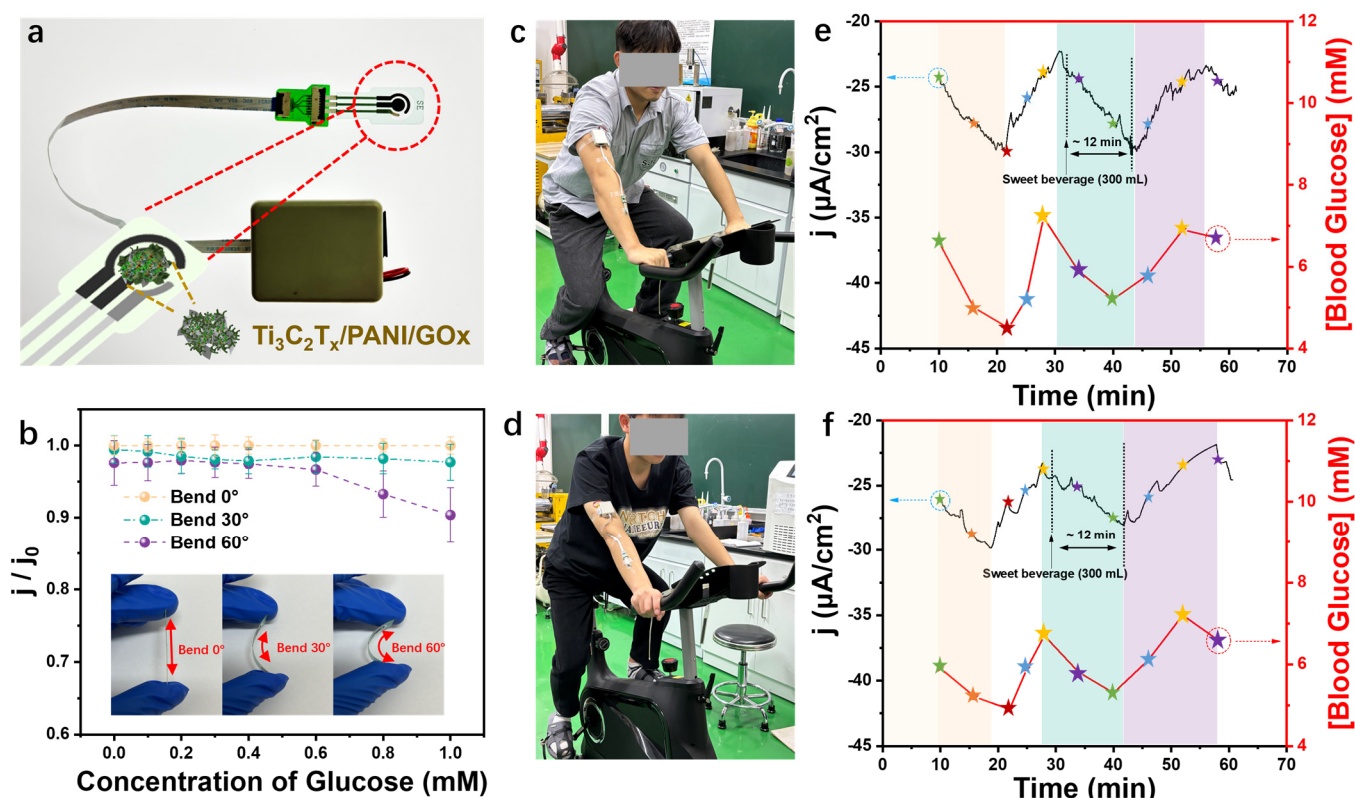

Figure 6. (**a**) The digital photo of the $Ti_3C_2T_x$/PANI/GOx glucose sensor; (**b**) the sensing performance of the $Ti_3C_2T_x$/PANI/GOx sensor after bent; (**c**,**d**) the photographs of the wearable $Ti_3C_2T_x$/PANI/GOx sensing device for on-body monitoring of sweat glucose; and (**e**,**f**) continuous real-time monitoring of the concentration levels of glucose of the corresponding subjects through an on-body sensing platform vs. blood glucose.

To verify the feasibility of the $Ti_3C_2T_x$/PANI/GOx chip for long-term and real-time monitoring of glucose concentration in authentic human sweat, two healthy and young subjects were recruited to engage in 60 min of indoor exercise for subsequent sweat analysis (Figure 6c,d). The real-time human sweat testing data corresponding to the subject's glucose response is depicted in Figure 6e,f. Meanwhile, the blood glucose levels for each subject were measured by a commercial glucose meter at a certain time interval. During the first 10 min of the exercise, no current fluctuations were recorded to ensure that enough sweat was collected. After exercise for 10 min, the change in current density reflected the change in glucose content in the sweat. Approximately 20 min post-exercise, both sweat glucose concentration and blood glucose concentration demonstrated a decline followed by an increase, attributed to the utilization of blood glucose in energy provision during

exercise, resulting in reduced concentration levels. Subsequently, hepatic glycogen breakdown occurred, leading to an elevation in blood glucose levels. Notably, the variation in blood glucose concentration had a direct impact on the variation observed in sweat glucose concentration [52]. With continuous exercise for 30 min, a 300 mL sweet beverage was consumed for each subject. The second decline in current density might be linked to the uptake of glucose by muscles during exercise [53]. It is noteworthy that the increase in sweat glucose levels after consuming sweet beverages does not occur immediately, but rather occurs 12 min later. A previous study indicated that the absorption of sugar from beverages by the intestine is within a timeframe from 10 to 15 min [54]. Following nearly an hour of exercise, both blood glucose and sweat glucose levels subsequently decreased. Throughout the entire process of exercise, the discrete results of blood glucose levels obtained from a commercial glucose meter exhibited a similar trend to the real-time monitoring of sweat glucose levels. Furthermore, to compare the accuracy of the fabricated sensor, the artificial sweat samples in different glucose concentrations were analyzed by the $Ti_3C_2T_x$/PANI/GOx sensor and HPLC (Figure S6). The fabricated $Ti_3C_2T_x$/PANI/GOx sensor demonstrated agreement with HPLC findings regarding the actual concentration of added glucose. The results exhibit a high level of concordance, indicating the accurate detection capability of the fabricated sensor. These above results demonstrate that a $Ti_3C_2T_x$/PANI/GOx flexible glucose sensor can be used for the precise and reliable detection of glucose in sweat.

4. Conclusions

In conclusion, we fabricated a binary nanocomposite $Ti_3C_2T_x$/PANI for GOx immobilization and on-body reliable sweat glucose monitoring. The coral-like biomimetic structure of PANI was achieved by an aniline monomer electropolymerized on the $Ti_3C_2T_x$ surface. This structure effectively reduces the stacking of $Ti_3C_2T_x$ nanoplates and enhances the enzyme immobilization efficiency. Based on the high conductivity and enhanced catalytic properties of $Ti_3C_2T_x$/PANI, the sensing performance of the $Ti_3C_2T_x$/PANI/GOx glucose sensor was further optimized. The $Ti_3C_2T_x$/PANI/GOx sensor demonstrated a high sensitivity of 26.04 $\mu A \cdot mM^{-1} \cdot cm^{-2}$ and 25.16 $\mu A \cdot mM^{-1} \cdot cm^{-2}$ for glucose detection in PBS and artificial sweat, respectively. In addition, the fabricated $Ti_3C_2T_x$/PANI/GOx sensor also showed excellent anti-interference performance, bending resistance, and long-term stability in glucose detection. We constructed an integrated wearable electrochemistry sweat glucose sensor based on $Ti_3C_2T_x$/PANI/GOx for real-time on-body sweat glucose monitoring during exercise. Simultaneously, the monitoring of glucose levels in the subjects during aerobic exercise involved a comprehensive comparison with the blood glucose levels. The discrete results of blood glucose levels obtained from a commercial glucose meter exhibited a similar trend to the real-time monitoring of sweat glucose levels. Furthermore, the comparative results reveal a high similarity between the $Ti_3C_2T_x$/PANI/GOx sensor and HPLC for glucose detection in artificial sweat. This flexible glucose biosensor based on $Ti_3C_2T_x$/PANI binary nanocomposite offers a promising approach for non-invasive and continuous glucose monitoring in healthcare.

References

1. Domingueti, C.P.; Dusse, L.M.; Carvalho, M.; de Sousa, L.P.; Gomes, K.B.; Fernandes, A.P. Diabetes mellitus: The linkage between oxidative stress, inflammation, hypercoagulability and vascular complications. *J. Diabetes Complicat.* **2016**, *30*, 738–745. [CrossRef] [PubMed]
2. Saeedi, P.; Petersohn, I.; Salpea, P.; Malanda, B.; Karuranga, S.; Unwin, N.; Colagiuri, S.; Guariguata, L.; Motala, A.A.; Ogurtsova, K.; et al. Global and regional diabetes prevalence estimates for 2019 and projections for 2030 and 2045: Results from the International Diabetes Federation Diabetes Atlas, 9th edition. *Diabetes Res. Clin. Pract.* **2019**, *157*, 107843. [CrossRef] [PubMed]
3. Xu, C.; Jiang, D.; Ge, Y.; Huang, L.; Xiao, Y.; Ren, X.; Liu, X.; Zhang, Q.; Wang, Y. A PEDOT:PSS conductive hydrogel incorporated with Prussian blue nanoparticles for wearable and noninvasive monitoring of glucose. *Chem. Eng. J.* **2022**, *431*, 134109. [CrossRef]
4. Jiang, D.; Zhang, Q.; Xu, C.; Ge, Y.; Huang, L.; Ren, X.; Wang, Y. Facile preparation of a hollow core-shell nanocomposite for the ultrasensitive sensing of glucose. *Sens. Actuators B Chem.* **2020**, *321*, 128500. [CrossRef]
5. Yao, Y.; Chen, J.; Guo, Y.; Lv, T.; Chen, Z.; Li, N.; Cao, S.; Chen, B.; Chen, T. Integration of interstitial fluid extraction and glucose detection in one device for wearable non-invasive blood glucose sensors. *Biosens. Bioelectron.* **2021**, *179*, 113078. [CrossRef] [PubMed]
6. Beck, R.W.; Bergenstal, R.M.; Laffel, L.M.; Pickup, J.C. Advances in technology for management of type 1 diabetes. *Lancet* **2019**, *394*, 1265–1273. [CrossRef] [PubMed]
7. Lee, H.; Hong, Y.J.; Baik, S.; Hyeon, T.; Kim, D.-H. Enzyme-Based Glucose Sensor: From Invasive to Wearable Device. *Adv. Healthc.* **2018**, *7*, 1701150. [CrossRef]
8. Myndrul, V.; Coy, E.; Babayevska, N.; Zahorodna, V.; Balitskyi, V.; Baginskiy, I.; Gogotsi, O.; Bechelany, M.; Giardi, M.T.; Iatsunskyi, I. MXene nanoflakes decorating ZnO tetrapods for enhanced performance of skin-attachable stretchable enzymatic electrochemical glucose sensor. *Biosens. Bioelectron.* **2022**, *207*, 114141. [CrossRef]
9. Zhang, S.; Liu, C.; Sun, X.; Huang, W. Current development of materials science and engineering towards epidermal sensors. *Prog. Mater. Sci.* **2022**, *128*, 100962. [CrossRef]
10. Wei, M.; Qiao, Y.; Zhao, H.; Liang, J.; Li, T.; Luo, Y.; Lu, S.; Shi, X.; Lu, W.; Sun, X. Electrochemical non-enzymatic glucose sensors: Recent progress and perspectives. *Chem. Comm.* **2020**, *56*, 14553–14569. [CrossRef]
11. Moyer, J.; Wilson, D.; Finkelshtein, I.; Wong, B.; Potts, R. Correlation Between Sweat Glucose and Blood Glucose in Subjects with Diabetes. *Diabetes Technol. Ther.* **2012**, *14*, 398–402. [CrossRef] [PubMed]
12. Gao, Y.; Huang, Y.; Ge, J.; Sun, L.; Zhou, A.; Feng, S.; Xu, Y.; Ning, X. An interrelated CataFlower enzyme system for sensitively monitoring sweat glucose. *Talanta* **2021**, *235*, 122799. [CrossRef] [PubMed]
13. Feng, L.; Qin, W.; Wang, Y.; Gu, C.; Li, X.; Chen, J.; Chen, J.; Qiao, H.; Yang, M.; Tian, Z.; et al. $Ti_3C_2T_x$ MXene/Graphene/AuNPs 3D porous composites for high sensitivity and fast response glucose biosensing. *Microchem. J.* **2023**, *184*, 108142. [CrossRef]
14. Cao, B.; Li, M.; Zhao, Y.; Zhou, H.; Tang, T.; Li, M.; Song, C.; Zhuang, W. Ultrathin 2D-MOFs for dual-enzyme cascade biocatalysis with sensitive glucose detection performances. *Colloids Surf. B Biointerfaces* **2023**, *230*, 113519. [CrossRef] [PubMed]

15. Jara Fornerod, M.J.; Alvarez-Fernandez, A.; Michalska, M.; Papakonstantinou, I.; Guldin, S. Glucose Oxidase Loading in Ordered Porous Aluminosilicates: Exploring the Potential of Surface Modification for Electrochemical Glucose Sensing. *Chem. Mater.* **2023**, *35*, 7577–7587. [CrossRef] [PubMed]

16. Kim, G.J.; Yoon, K.J.; Kim, K.O. Glucose-responsive poly(vinyl alcohol)/β-cyclodextrin hydrogel with glucose oxidase immobilization. *J. Mater. Sci.* **2019**, *54*, 12806–12817. [CrossRef]

17. Lin, Y.-C.; Rinawati, M.; Chang, L.-Y.; Wang, Y.-X.; Wu, Y.-T.; Yen, Y.-H.; Chen, K.-J.; Ho, K.-C.; Yeh, M.-H. A non-invasive wearable sweat biosensor with a flexible N-GQDs/PANI nanocomposite layer for glucose monitoring. *Sens. Actuators B Chem.* **2023**, *383*, 133617. [CrossRef]

18. Hao, L.; Li, S.-S.; Wang, J.; Tan, Y.; Bai, L.; Liu, A. MnO_2/multi-walled carbon nanotubes based nanocomposite with enhanced electrocatalytic activity for sensitive amperometric glucose biosensing. *J. Electroanal. Chem.* **2020**, *878*, 114602. [CrossRef]

19. Hui, X.; Sharifuzzaman, M.; Sharma, S.; Xuan, X.; Zhang, S.; Ko, S.G.; Yoon, S.H.; Park, J.Y. High-Performance Flexible Electrochemical Heavy Metal Sensor Based on Layer-by-Layer Assembly of Ti3C2Tx/MWNTs Nanocomposites for Noninvasive Detection of Copper and Zinc Ions in Human Biofluids. *ACS Appl. Mater.* **2020**, *12*, 48928–48937. [CrossRef]

20. Naguib, M.; Kurtoglu, M.; Presser, V.; Lu, J.; Niu, J.; Heon, M.; Hultman, L.; Gogotsi, Y.; Barsoum, M.W. Two-Dimensional Nanocrystals Produced by Exfoliation of Ti_3AlC_2. *Adv. Mater.* **2011**, *23*, 4248–4253. [CrossRef]

21. Chen, F.; Wang, J.; Chen, L.; Lin, H.; Han, D.; Bao, Y.; Wang, W.; Niu, L. A Wearable Electrochemical Biosensor Utilizing Functionalized $Ti_3C_2T_x$ MXene for the Real-Time Monitoring of Uric Acid Metabolite. *Anal. Chem.* **2024**, *96*, 3914–3924. [CrossRef] [PubMed]

22. Anasori, B.; Lukatskaya, M.R.; Gogotsi, Y. 2D metal carbides and nitrides (MXenes) for energy storage. *Nat. Rev. Mater.* **2017**, *2*, 16098. [CrossRef]

23. Zheng, W.; Zhang, P.; Chen, J.; Tian, W.B.; Zhang, Y.M.; Sun, Z.M. In situ synthesis of CNTs@Ti3C2 hybrid structures by microwave irradiation for high-performance anodes in lithium ion batteries. *J. Mater. Chem. A.* **2018**, *6*, 3543–3551. [CrossRef]

24. Zhao, M.-Q.; Ren, C.E.; Ling, Z.; Lukatskaya, M.R.; Zhang, C.; Van Aken, K.L.; Barsoum, M.W.; Gogotsi, Y. Flexible MXene/Carbon Nanotube Composite Paper with High Volumetric Capacitance. *Adv. Mater.* **2015**, *27*, 339–345. [CrossRef]

25. Zhang, S.; Zahed, M.A.; Sharifuzzaman, M.; Yoon, S.; Hui, X.; Chandra Barman, S.; Sharma, S.; Yoon, H.S.; Park, C.; Park, J.Y. A wearable battery-free wireless and skin-interfaced microfluidics integrated electrochemical sensing patch for on-site biomarkers monitoring in human perspiration. *Biosens. Bioelectron.* **2021**, *175*, 112844. [CrossRef]

26. Ding, H.; Jiang, D.; Du, X.; Zhang, Z.; Jiang, J.; Shan, X.; Wang, W.; Shiigi, H.; Chen, Z. Hydrovoltaic Effect Coupling with Capacitor Amplification: A Mode for Sensitive Self-Powered Electrochemical Sensing. *Anal. Chem.* **2023**, *95*, 12595–12599. [CrossRef]

27. Liu, Y.; Yang, Y.; Deng, B.; Jing, L.; Yin, B.; Yang, M. Vertically aligned polyaniline nano-array decorated on ultra-thin MXene nanosheets for high energy density supercapacitors. *J. Energy Storage.* **2022**, *56*, 105893. [CrossRef]

28. Cai, Y.-Z.; Fang, Y.-S.; Cao, W.-Q.; He, P.; Cao, M.-S. MXene-CNT/PANI ternary material with excellent supercapacitive performance driven by synergy. *J. Alloys Compd.* **2021**, *868*, 159159. [CrossRef]

29. Sarycheva, A.; Gogotsi, Y. Raman Spectroscopy Analysis of the Structure and Surface Chemistry of $Ti_3C_2T_x$ MXene. *Chem. Mater.* **2020**, *32*, 3480–3488. [CrossRef]

30. Wu, G.; Du, H.; Pakravan, K.; Kim, W.; Cha, Y.L.; Chiang, S.-T.; Beidaghi, M.; Zhang, X.; Kim, S.H.; Pan, X.; et al. Polyaniline/Ti3C2Tx functionalized mask sensors for monitoring of CO_2 and human respiration rate. *Chem. Eng. J.* **2023**, *475*, 146228. [CrossRef]

31. Kim, S.J.; Koh, H.-J.; Ren, C.E.; Kwon, O.; Maleski, K.; Cho, S.-Y.; Anasori, B.; Kim, C.-K.; Choi, Y.-K.; Kim, J.; et al. Metallic $Ti_3C_2T_x$ MXene Gas Sensors with Ultrahigh Signal-to-Noise Ratio. *ACS Nano* **2018**, *12*, 986–993. [CrossRef] [PubMed]

32. Li, C.; Xu, J.; Xu, Q.; Xue, G.; Yu, H.; Wang, X.; Lu, J.; Cui, G.; Gu, G. Synthesis of Ti_3C_2 MXene@PANI composites for excellent anticorrosion performance of waterborne epoxy coating. *Prog. Org. Coat.* **2022**, *165*, 106673. [CrossRef]

33. Qiu, H.; Qu, X.; Zhang, Y.; Chen, S.; Shen, Y. Robust PANI@MXene/GQDs-Based Fiber Fabric Electrodes via Microfluidic Wet-Fusing Spinning Chemistry. *Adv. Mater.* **2023**, *35*, 2302326. [CrossRef] [PubMed]

34. Li, X.; Xu, J.; Jiang, Y.; He, Z.; Liu, B.; Xie, H.; Li, H.; Li, Z.; Wang, Y.; Tai, H. Toward agricultural ammonia volatilization monitoring: A flexible polyaniline/$Ti_3C_2T_x$ hybrid sensitive films based gas sensor. *Sens. Actuators B Chem.* **2020**, *316*, 128144. [CrossRef]

35. Yang, R.; Zhang, J.; Liu, J.; Li, G.; Qiao, Y.; Zhang, X.; Gao, J.; Lu, H. PANI/Ti3C2Tx composite nanofiber-based flexible conductometric sensor for the detection of NH_3 at room temperature. *Sens. Actuators B Chem.* **2023**, *392*, 134128. [CrossRef]

36. Hu, F.; Chen, S.; Wang, C.; Yuan, R.; Chai, Y.; Xiang, Y.; Wang, C. ZnO nanoparticle and multiwalled carbon nanotubes for glucose oxidase direct electron transfer and electrocatalytic activity investigation. *J. Mol. Catal.* **2011**, *72*, 298–304. [CrossRef]

37. Tian, K.; Alex, S.; Siegel, G.; Tiwari, A. Enzymatic glucose sensor based on Au nanoparticle and plant-like ZnO film modified electrode. *Mater. Sci. Eng. C.* **2015**, *46*, 548–552. [CrossRef]

38. Laviron, E. General expression of the linear potential sweep voltammogram in the case of diffusionless electrochemical systems. *J. Electroanal. Chem. Interfacial Electrochem.* **1979**, *101*, 19–28. [CrossRef]

39. Zhou, F.; Jing, W.; Xu, Y.; Chen, Z.; Jiang, Z.; Wei, Z. Performance enhancement of ZnO nanorod-based enzymatic glucose sensor via reduced graphene oxide deposition and UV irradiation. *Sens. Actuators B Chem.* **2019**, *284*, 377–385. [CrossRef]

40. Kim, J.Y.; Jo, S.-Y.; Sun, G.-J.; Katoch, A.; Choi, S.-W.; Kim, S.S. Tailoring the surface area of ZnO nanorods for improved performance in glucose sensors. *Sens. Actuators B Chem.* **2014**, *192*, 216–220. [CrossRef]

41. Oh, S.Y.; Hong, S.Y.; Jeong, Y.R.; Yun, J.; Park, H.; Jin, S.W.; Lee, G.; Oh, J.H.; Lee, H.; Lee, S.-S.; et al. Skin-Attachable, Stretchable Electrochemical Sweat Sensor for Glucose and pH Detection. *ACS Appl. Mater.* **2018**, *10*, 13729–13740. [CrossRef] [PubMed]

42. Li, X.; Zhao, C.; Liu, X. A paper-based microfluidic biosensor integrating zinc oxide nanowires for electrochemical glucose detection. *Microsyst. Nanoeng.* **2015**, *1*, 15014. [CrossRef]

43. Phetsang, S.; Jakmunee, J.; Mungkornasawakul, P.; Laocharoensuk, R.; Ounnunkad, K. Sensitive amperometric biosensors for detection of glucose and cholesterol using a platinum/reduced graphene oxide/poly(3-aminobenzoic acid) film-modified screen-printed carbon electrode. *Bioelectrochemistry* **2019**, *127*, 125–135. [CrossRef] [PubMed]

44. Liu, Y.; Zhang, X.; He, D.; Ma, F.; Fu, Q.; Hu, Y. An amperometric glucose biosensor based on a MnO_2/graphene composite modified electrode. *RSC Advances* **2016**, *6*, 18654–18661. [CrossRef]

45. Lee, H.; Choi, T.K.; Lee, Y.B.; Cho, H.R.; Ghaffari, R.; Wang, L.; Choi, H.J.; Chung, T.D.; Lu, N.; Hyeon, T.; et al. A graphene-based electrochemical device with thermoresponsive microneedles for diabetes monitoring and therapy. *Nat. Nanotechnol.* **2016**, *11*, 566–572. [CrossRef]

46. Hozumi, S.; Honda, S.; Arie, T.; Akita, S.; Takei, K. Multimodal Wearable Sensor Sheet for Health-Related Chemical and Physical Monitoring. *ACS Sens.* **2021**, *6*, 1918–1924. [CrossRef]

47. Liao, Q.-L.; Jiang, H.; Zhang, X.-W.; Qiu, Q.-F.; Tang, Y.; Yang, X.-K.; Liu, Y.-L.; Huang, W.-H. A single nanowire sensor for intracellular glucose detection. *Nanoscale* **2019**, *11*, 10702–10708. [CrossRef]

48. Li, B.; Wu, X.; Shi, C.; Dai, Y.; Zhang, J.; Liu, W.; Wu, C.; Zhang, Y.; Huang, X.; Zeng, W. Flexible enzymatic biosensor based on graphene sponge for glucose detection in human sweat. *Surf. Interfaces* **2023**, *36*, 102525. [CrossRef]

49. Mansouri, N.; Babadi, A.A.; Bagheri, S.; Hamid, S.B.A. Immobilization of glucose oxidase on 3D graphene thin film: Novel glucose bioanalytical sensing platform. *Int. J. Hydrogen Energy.* **2017**, *42*, 1337–1343. [CrossRef]

50. Gao, W.; Emaminejad, S.; Nyein, H.Y.Y.; Challa, S.; Chen, K.; Peck, A.; Fahad, H.M.; Ota, H.; Shiraki, H.; Kiriya, D.; et al. Fully integrated wearable sensor arrays for multiplexed in situ perspiration analysis. *Nature* **2016**, *529*, 509–514. [CrossRef]

51. Jobst, G.; Moser, I.; Varahram, M.; Svasek, P.; Aschauer, E.; Trajanoski, Z.; Wach, P.; Kotanko, P.; Skrabal, F.; Urban, G. Thin-Film Microbiosensors for Glucose−Lactate Monitoring. *Anal. Chem.* **1996**, *68*, 3173–3179. [CrossRef] [PubMed]

52. Liu, D.; Liu, Z.; Feng, S.; Gao, Z.; Chen, R.; Cai, G.; Bian, S. Wearable Microfluidic Sweat Chip for Detection of Sweat Glucose and pH in Long-Distance Running Exercise. *Biosensors* **2023**, *13*, 157. [CrossRef] [PubMed]

53. Sylow, L.; Kleinert, M.; Richter, E.A.; Jensen, T.E. Exercise-stimulated glucose uptake—Regulation and implications for glycaemic control. *Nat. Rev. Endocrinol.* **2017**, *13*, 133–148. [CrossRef] [PubMed]

54. Wolever, T.M.S. Carbohydrate and the Regulation of Blood Glucose and Metabolism. *Nutr. Rev.* **2003**, *61* (Suppl. S5), S40–S48. [CrossRef]